


Switching from electromagnetic to chemical mechanism in quantum plasmonic tip-induced graphene oxide enhanced Raman scattering

Hana N. Hrim,^{1,*} Sharad Ambardar,² Abdullah Albagami,^{1,3} Simon Mendenhall,¹ M. Tuan Trinh,^{1,4} and Dmitri V. Voronine ^{1,2,†}

¹*Department of Physics, University of South Florida, Tampa, Florida 33620, USA*

²*Department of Medical Engineering, University of South Florida, Tampa, Florida 33620, USA*

³*Department of Physics, King Saud University, Riyadh 11362, Kingdom of Saudi Arabia*

⁴*Department of Chemistry and Biochemistry, Utah State University, Logan, Utah 84322, USA*



(Received 17 December 2021; revised 19 June 2022; accepted 27 June 2022; published 11 July 2022)

Surface-enhanced Raman scattering (SERS) is based on the ability of a surface substrate to increase Raman signals for sensing and imaging applications. The most widely used Au and Ag SERS substrates are primarily based on the electromagnetic mechanism (EM) with large enhancement factors (EFs), which are, however, limited by small gaps due to tunneling. Graphene has been explored as an alternative substrate for graphene-enhanced Raman scattering based on the chemical mechanism (CM). However, the limits of CM EFs in graphene-based substrates have not been well understood, especially as a function of tip-sample distance (TSD). Here we performed tip-enhanced Raman scattering of carbon nanotubes on Au and graphene-oxide (GO) hybrid substrates for different TSDs. We show evidence of quantum plasmonics with GO as a tunneling junction in an Au-GO-Au cavity with a 2-nm gap size. We demonstrate Raman signal enhancement by four orders of magnitude beyond the EM tunneling limit by switching to the CM regime for the resonant GO excitation at small TSD. Tip-induced GO-enhanced Raman scattering may be used to improve nanoimaging and biosensing on novel hybrid GO/Au substrates.

DOI: [10.1103/PhysRevB.106.035410](https://doi.org/10.1103/PhysRevB.106.035410)

I. INTRODUCTION

Surface-enhanced Raman scattering (SERS) is a minimally invasive spectroscopic technique for chemically specific detection with high sensitivity down to the single molecule level [1–3]. Impressive achievements of single molecule imaging with subnanometer spatial resolution using tip-enhanced Raman scattering (TERS) have recently been demonstrated [4–6]. However, the subnanoscale resolution has only been achieved for a few systems with large Raman scattering cross sections on pure metallic substrates. They involve simultaneous contributions of two enhancement mechanisms, electromagnetic (EM) [7–9] and chemical mechanism (CM) [10,11], which cannot be easily separated and therefore hinder the mechanistic understanding of single molecule sensitivity and imaging contrast.

The EM enhancement in plasmonic SERS is based on a large increase of local electromagnetic fields in the vicinity of metallic nanostructures that support surface plasmons [7–9]. The EM enhancement factors (EFs) can be $\sim 10^8 - 10^{12}$ due to the fourth order near field dependence. The strongest near fields are obtained in rough Ag nanostructures and may be tuned by morphology, size, and surface composition. Electromagnetic hot spots are localized areas in the gaps between plasmonic nanoparticles that generate the largest EM EFs. Numerous studies have been performed to optimize the SERS

efficiency of noble metal plasmonic systems. Surface plasmon resonance and gap size were optimized to increase the hot spot intensity [12–15]. The gap size between plasmonic nanoparticles in SERS corresponds to tip-sample distance (TSD) in TERS. Classically, the smaller TSD or gap size leads to stronger hot spots. However, there is a fundamental limit of the maximum signal that can be achieved by the EM.

Quantum effects, such as tunneling and nonlocality, play an important role in plasmonic systems when the gap size is reduced. The classical descriptions of surface plasmon energy, linewidth, and field enhancement break down, and the full quantum mechanical treatment is necessary [15–24]. In this quantum plasmonic regime, tunneling at small TSD leads to the reduction of surface charge density and the corresponding near field intensity. Therefore, after the optimal balance of EM enhancement and tunneling suppression, further reduction of TSD leads to the quenching of the TERS signal. This specific value of TSD sets the quantum tunneling limit to SERS and TERS that have traditionally been accepted as “ultimate” [25]. Several experimental demonstrations revealed this tunneling limit of SERS signals for gaps smaller than ~ 1 nm [12,20]. Similar limits were shown in TSD dependence studies of TERS and tip-enhanced photoluminescence (TEPL) [21]. Recent work showed that tunneling may take place even for gap size above 1 nm for certain molecular spacers in the plasmonic gap [26–29]. For example, DNA spacers with size up to 2.8 nm were shown to support tunneling in plasmonic dimers [29]. Direct tunneling depends on the gap size and barrier height [30]. They can be modified by the large electric field in the gap via the

*Corresponding author: nazari.hana118@gmail.com

†Corresponding author: dmitri.voronine@gmail.com

Fowler-Nordheim (FN) tunneling mechanism [26–28]. However, the EM enhancement is still limited even in the FN tunneling regime, where the classical-to-quantum transition takes place at a larger TSD. These quantum plasmonic effects have been mainly investigated in systems based on the EM enhancement. However, neither SERS gap-size dependence nor TERS TSD dependence has been thoroughly investigated in nonplasmonic CM-based systems. Therefore, the limits of CM enhancement in graphene-enhanced Raman scattering (GERS) and hybrid SERS platforms have not been well understood.

The CM enhancement is based on analyte-substrate chemical interactions, such as charge transfer (CT) between various analyte and substrate states, which can modify the analyte polarizability and increase the Raman scattering cross section [31–33]. The CM EFs can be $\sim 10 - 10^2$ or higher if special substrates or synergistic effects are involved. Photoinduced resonance CT is a type of CM where the excitation wavelength is resonant with the CT transition between the analyte and substrate. Resonance CT EFs of $\sim 10^3 - 10^4$ were previously reported [34–36]. While the EM is dominant for metallic substrates in the hot spots, the CM is dominant in nonmetallic plasmon-free substrates, which are suitable for biological applications due to high biocompatibility. However, the plasmon-free CM enhancement is smaller than the plasmonic EM. This inspired the search for new hybrid SERS substrates with optimized properties based on the interplay of the two mechanisms.

Graphene is a promising two-dimensional (2D) substrate for SERS applications with large flexibility and good mechanical stability, in the so-called graphene-enhanced Raman scattering (GERS) [37–40]. A functionalized graphene, namely graphene oxide (GO), has recently been used as a GERS substrate and showed larger EFs than pristine graphene, which was attributed to the CM enhancement on GO [38,41–45]. GO-based substrates have biological compatibility, high thermal and chemical stability [45], and can be fabricated with a high yield and low cost. Moreover, the large surface area of GO helps adsorbing organic aromatic molecules [46], polymers [47], and ions [48]. These properties make GO a useful substrate for the construction of novel hybrid SERS platforms. GO-enhanced Raman scattering is mainly due to the CM mechanism involving charge transfer [49]. However, compared with noble metallic SERS substrates, GO showed smaller EFs of $\sim 10^3$. A combination of GO with a plasmonic system with EM enhancement, a hybrid GO-metallic system, would boost a higher EF.

Here, we show that a hybrid GO/Au substrate can be used to largely enhance the TERS signal at a smaller TSD beyond the EM tunneling limit. We performed TSD measurements in a hybrid Au-GO-Au plasmonic cavity which provides two controllable gaps and enables the precise gap control with sub-nm resolution for tuning the Raman response. Surprisingly, we discovered a large signal enhancement (more than four orders of magnitude) from carbon nanotubes (CNTs) on GO/Au substrates in the quantum plasmonic regime surpassing the enhancement values of the traditional quantum plasmonic EM tunneling limit. Our results show the separation of the EM and CM enhancements via the TSD control in a hybrid GO/Au system. This opens new opportunities to

perform subnanoscale imaging of a wide range of molecular systems and investigate and control the complex interplay of enhancement mechanisms to further improve sensitivity and resolution.

A. Experimental setup

The sketch of tip-induced GO-enhanced Raman scattering (TIGERS) experimental setup is shown in Fig. 1. The laser illumination of the Au-coated SPM tip results in the formation of a near-field hot spot at the tip apex with ~ 10 nm size corresponding to the tip radius. Figure 1(a) shows the classical plasmonic regime with a large TSD gap (gap 1 > 0.36 nm), which corresponds to the van der Waals (vdW) contact distance between the Au tip and Au surface [12]. The second gap, which corresponds to the vdW contact distance between the GO and CNT gap2 = 0.32 nm, was estimated using the vdW radii of ~ 0.17 and ~ 0.15 nm for C and O, respectively. Both gaps were measured using the same approach by fitting the linear piezo position dependence of the repulsive force as described below. The only difference is that we used different vdW radii, namely, those of C and O atoms for gap 2, and C and Au atoms for gap 1, because gap 2 is a contact between CNT and GO, while gap 1 is a contact between CNT and Au. The large hot spot size [green shaded area directly under the tip in Fig. 1(a)] corresponds to a strong hot spot due to the EM enhancement. The contribution of the CM enhancement between the Au tip and sample is weaker compared to the EM and is not shown. On the other hand, the CM enhancement due to the interaction between GO and CNT is stronger due to the GERS effect [red shaded area between CNT and GO in Fig. 1(a)]. However, the CM enhancement of GERS is still weaker than the EM enhancement of TERS in the classical regime [the green area above CNT is larger than the red area below CNT in Fig. 1(a)].

Further pushing the tip on the sample by applying the force beyond the vdW contact distance leads to the decrease of both gaps, gap 1 and gap 2, and the corresponding decrease of the EM hot spot (above CNT) and the increase of the CM “hot spot” (below CNT) due to charge transfer via the quantum tunneling [Fig. 1(b)]. The experimental realization is obtained in our setup based on the contact mode atomic force microscopy (AFM), that was previously described [50,51]. Briefly, the tip and laser are kept stationary during the measurements, while the sample stage is approached with ~ 0.16 nm piezo stage precision in the commercial TERS setup (Horiba Scientific). All experiments were performed under ambient conditions at room temperature. AFM and far-field Raman measurements were performed in tapping mode with 20-nm average TSD. TERS measurements were performed in contact mode with 0.36-nm TSD. AFM and Raman imaging were performed using a confocal microscope (XPlora, Horiba) coupled to a scanning probe microscope (OmegaScopeR, Horiba) with 532- and 638-nm cw lasers focused using an objective lens (numerical aperture = 0.9) on the Au-coated Ag tip with the tip apex radius of ~ 10 nm (Horiba Scientific). We checked the tip for thermal damage after every experiment by measuring the PL signal from the tip itself in the air. No significant changes in the PL signal from the tip were observed. We typically use this weak PL signal for the tip-laser overlap

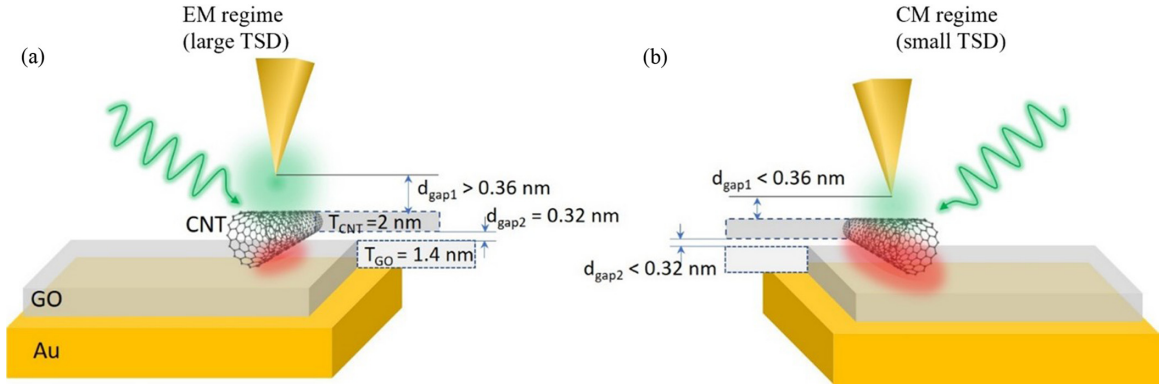


FIG. 1. Tip-induced GO-enhanced Raman scattering (TIGERS) experiment in EM (a) and CM (b) regimes. (a) EM regime with large tip-sample distance (TSD) gap 1 > 0.36 nm with a strong electromagnetic (EM) hot spot (green shaded area directly under the tip) and gap 2 = 0.32 nm with a weak chemical (CM) hot spot (red shaded area directly under CNT). (b) CM regime with a small TSD gap 1 < 0.36 nm with a weak EM hot spot and a small gap 2 < 0.32 nm with a strong CM hot spot.

alignment. Ag provides a stronger enhancement compared to Au. We used a thin 3–5-nm coating of Au to protect Ag from oxidation. Absorption is minimized in such a thin layer of Au, and it is not expected to cause any significant thermal damage. We refer to our tip as a Au tip for simplicity below.

The radius of the laser focal spot was ~ 500 nm. Using a backscattering configuration with 532- and 638-nm edge filters, the scattered signals were collected and detected by a spectrometer with 600 g/mm grating coupled to a charge coupled device camera. TERS maps were obtained using acquisition time of 0.2 s and 0.5 mW laser power. The detailed setup for the TERS experiments was previously described [12]. The angle between the incident laser optical axis and the horizontal sample plane was 25° . The angle between the tip and the sample plane was 78° . The incident light polarization was along the tip axis. After the vdW contact, both tip and sample keep moving in response to the applied force by the tip, resulting in a gradual decrease of the actual TSD with sub-nm step size. We previously showed TSD control of Au PL with sub-nm precision in the quantum regime of TSD < 0.36 nm [12]. We observed quenching of Au PL for the decreasing of TSD due to tunneling, which corresponds to gap 1 in Figs. 1(a) and 1(b). Similarly, the CNT-GO gap 2 varies simultaneously with gap 1 during the tip-sample approach, leading to the increase of CNT Raman signals due to the CM mechanism.

We estimated $\Delta d \sim 10$ pm uncertainty of TSD measurements based on the error transfer analysis of the repulsive part of the Lennard-Jones model shown in Supplemental Material Fig. S2 [52] and described in detail in our previous work [12]. Briefly, we analyzed the linear piezo position dependence of the repulsive force (Fig. S2a) and obtained its deviation $\Delta f \sim 0.769$ nN. Then using the mean values of the repulsive force ($\bar{f} \sim 7$ nN) and TSD ($\bar{d} \sim 0.3$ nm) in the error transfer relation $|\frac{\Delta f}{f}| = 13|\frac{\Delta d}{d}|$, where the repulsive force $f = Ad^{-13}$, we obtained the corresponding TSD deviation (Fig. S2b). We varied the piezo stage position with 0.16 nm precision to obtain ~ 10 -pm TSD step size that was used in the measurements below.

We defined the tip-substrate gap as the distance between the Au tip and the Au substrate. This gap forms the plasmonic

cavity by coupling the localized surface plasmons of the Au tip with the image dipoles at the Au surface, forming so called gap-mode plasmons. This results in high intensity SERS hot spots. The total tip-substrate gap size for the GO-CNT system in the plasmonic cavity between the Au tip and Au substrate is the combination of the two gaps (gap 1 and gap 2) and the two thicknesses of CNT and GO, which at the vdW contact distance is $d_{\text{gap}} = d_{\text{gap1}} + d_{\text{gap2}} + T_{\text{CNT}} + T_{\text{GO}} = 0.36 + 0.32 + 2 + 1.4 = 4.08$ nm. Previously, we developed a phenomenological model of tunneling in 2D materials in plasmonic cavities with subnanometer gaps [12,17,53]. The present results indicate that tunneling takes place even with larger gap sizes, which could be explained by the FN-tunneling mechanism, described above [26–28]. We show evidence for such quantum plasmonic tunneling below, optimized by tuning the two variable gaps as control parameters.

B. Sample preparation

The solution of 70% metallic single-walled CNTs and GO flakes (Graphene Supermarket®) in ethanol was drop casted on atomically flat Au substrate (Ted Pella, Inc.) and dried. As a result, some CNTs were randomly placed on GO flakes. GO was chemically synthesized using the Hummers method [54,55]. Native GO is an insulator [56,57]. Therefore, we neglected its conductivity. Reduced GO (rGO), that could be obtained using various reduction methods, may have non-negligible conductivity but was not used in this work.

GO comprises a few-nanometers-thick sheet of carbon atoms bonded to functional groups, such as carboxyl, carbonyl, hydroxyl, etc. [45]. We measured the thickness of GO using AFM to be $d_{\text{GO}} = 1.4 \pm 0.1$ nm. The vdW gap between the Au tip and GO is $d_{\text{gap1}} = 0.3$ nm. This makes the total tip-substrate gap size $d_{\text{gap}} = 1.7$ nm.

II. RESULTS

A. TERS, GERS, and TIGERS with resonant (638 nm) excitation

First, we performed Raman scattering measurements at four different tip-sample-substrate configurations to

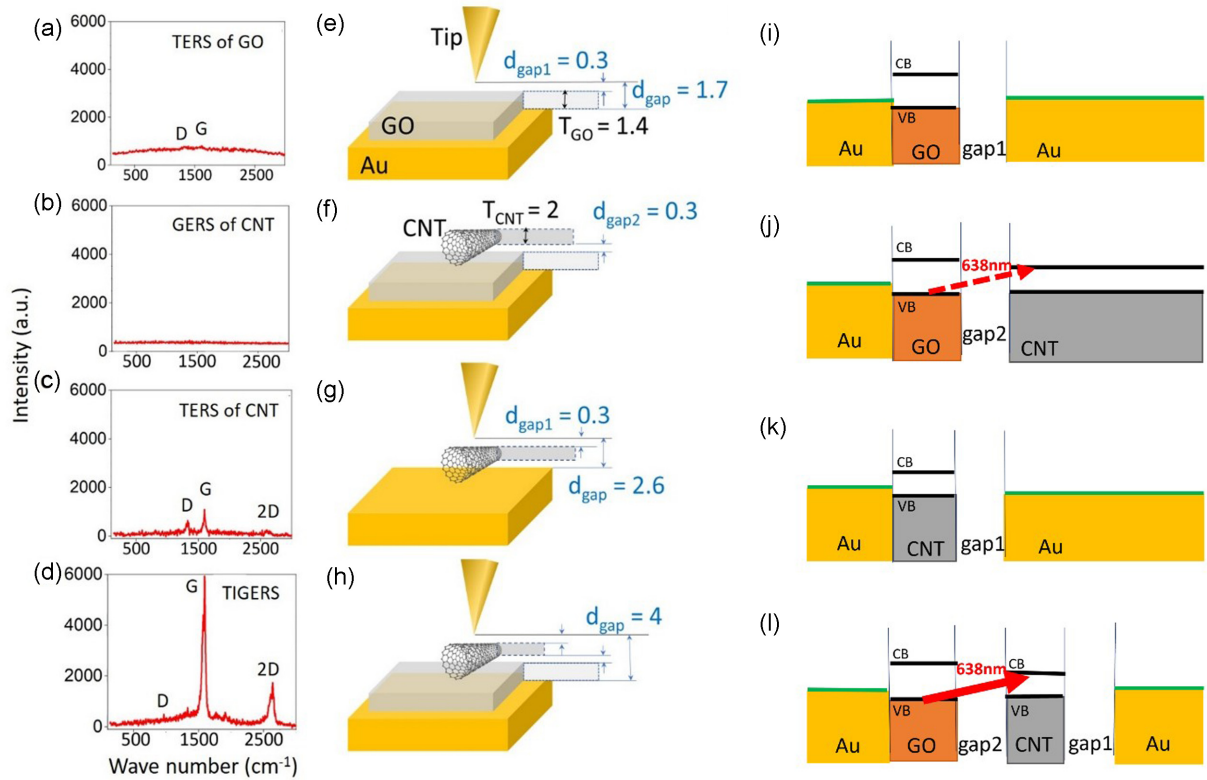


FIG. 2. Comparison of schematics, diagrams and spectra in TERS, GERS, and TIGERS experiments performed using 638-nm excitation: (a),(e),(i) TERS of GO; (b),(f),(j) GERS of CNT; (c),(g),(k) TERS of CNT; (d),(h),(l) TIGERS of CNT. Schematic experimental sketches (e)–(h) indicate gaps and sample thicknesses. The total gap between the Au tip and Au substrate d_{gap} is the sum of relevant gaps and sample thicknesses. Energy diagrams (i)–(l) show photoinduced charge transfer at 638-nm excitation (red arrows).

demonstrate the synergistic TIGERS enhancement. We used the 638-nm excitation, which is resonant with the GO-CNT complex. We obtained a large Raman signal enhancement of CNT on GO/Au substrate at short TSD in the quantum regime. We performed imaging, and compared different CNTs placed partially or completely on the GO flake.

The comparison of TERS, GERS, and TIGERS is shown in Fig. 2. Figures 2(a) and 2(d) show Raman intensity obtained in experiments that were performed using 638-nm excitation under the identical conditions with the same laser power. Figures 2(e)–2(h) show the experimental schematics of the specific tip-sample-substrate configurations, highlighting the relevant TSDs. Figures 2(i)–2(l) show the corresponding energy diagrams and enhancement mechanisms.

Figure 2(a) shows the TERS spectrum of GO, which under the chosen experimental conditions has weak signals from the *D* and *G* bands. TERS of graphene and GO were previously investigated [42,58]. TERS was used for nanoscale mapping of the *D* and *G* bands, which arise from the scattering by defects and E_{2g} modes, respectively [59].

Figures 2(c), 2(g), and 2(k) show the TERS of CNT on the Au substrate. The Raman signals of the *D* and *G* bands of CNT are stronger than of GO. The characteristic 2D band of CNT is also observed. Tunneling between the Au tip and Au substrate at small TSD reduces the Raman signals for both 532- and 638-nm excitations, via the EM mechanism. However, for 638 nm there is also additional CM enhancement due to the resonant excitation of the GO-CNT complex.

Figure 2(b) shows the GERS spectrum of CNT that was obtained without the Au tip. No Raman signals of CNT or GO were detectable under the chosen conditions. The GERS signal was weaker than TERS confirming the larger contribution of the EM mechanism compared to the CM mechanism. The CM mechanism of the GERS signal is shown by a dashed red arrow in Fig. 2(j).

Figure 2(d) shows the TIGERS spectrum of CNT on the same intensity scale as GERS and TERS spectra in Figs. 2(a)–2(c). The TIGERS signal is stronger than the combination of all these signals, showing a synergistic effect. The thick solid arrow in Fig. 2(l) indicates the enhanced CT contribution.

Figure 3(a) shows the schematic of the CNT sample on the GO/Au substrate, which includes three CNTs, one of which is on the Au substrate (CNT2), one is on GO/Au (CNT3), and one is partially placed on both substrates (CNT1). Figure 3(b) shows the corresponding AFM height image. The thick bright line in Fig. 3(b) is a GO wrinkle, that was confirmed by the large AFM height in Fig. 3(b) and a strong Raman signal in Fig. 3(d) (red line) showing the characteristic *D* (1350 cm^{-1}) and *G* (1585 cm^{-1}) bands of GO and the absence of the 2D (2600 cm^{-1}) band of CNT. It most likely originated from CNT3 in Fig. 3(b). TERS mapping of the *D* and 2D bands in Fig. 3(e) correlates with the AFM topography in Fig. 3(b). TERS imaging was performed with small TSD, shorter than the vdW contact which corresponds to the TIGERS diagram in Fig. 1(b) in the quantum regime. We used the 2D band to map CNTs, while using the *D* band to map both GO and CNTs.

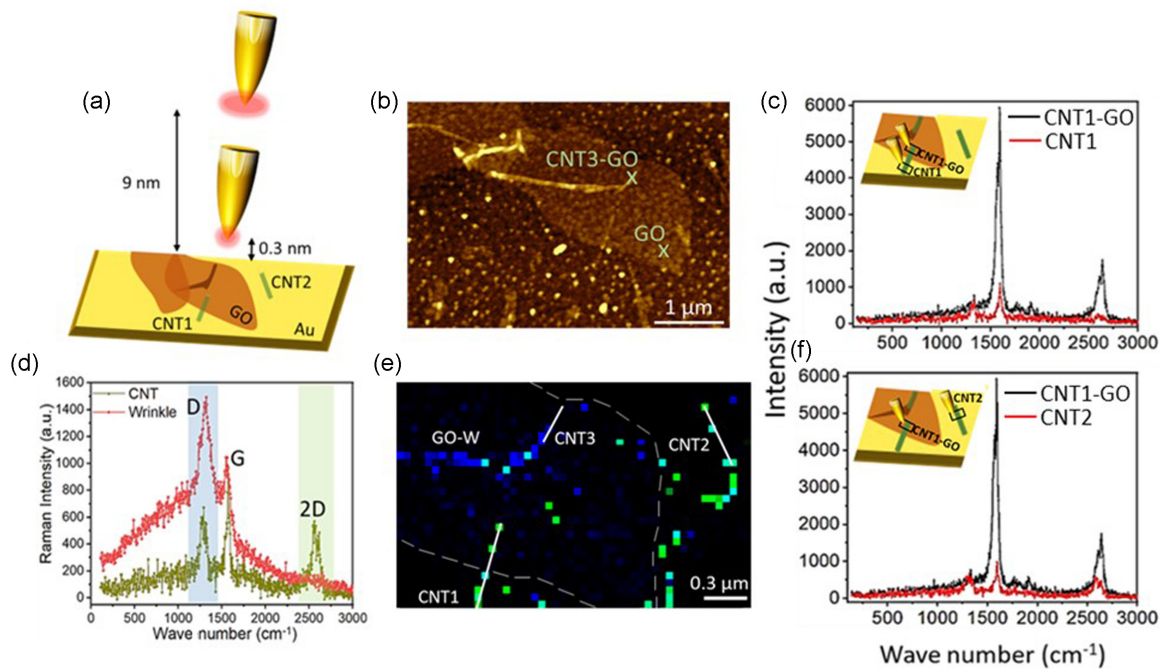


FIG. 3. (a) Schematic of tip-enhanced Raman imaging of the CNT sample on GO/Au substrate. Tip-sample distance (TSD) of 0.3 and 9 nm corresponds to the quantum and classical regimes, respectively. Near-field intensity at the tip apex decreases at a short gap due to the tunneling limit. (b) AFM height image of GO flakes and CNTs on Au substrate. GO and CNT3-GO mark the locations of absence and presence of CNT on GO, respectively. (c) Raman spectra from two different locations on the same CNT, partially on GO/Au (CNT1-GO) and on Au substrate (CNT1). (f) Raman spectra from two different CNTs, CNT1 on GO/Au and CNT2 on Au substrate. (d) Raman spectra of CNT (green) and GO wrinkle (red). (e) Overlapped Raman maps of the *D* (blue) and 2*D* (green) bands highlighted in (d) show images of three CNTs (CNT1, CNT2, and CNT3) and GO wrinkle (GO-W).

Mapping of the *D* band in Fig. 3(e) shows a stronger signal on GO wrinkles as compared to the pristine GO flake. This enhancement at the wrinkles is associated with the in-plane Raman modes distorted by wrinkles, leading to the out-of-plane signal enhancement due to the near-field projection along the plasmonic tip axis [58].

Figures 3(c) and 3(f) show the comparison of the TIGERS and TERS signals of CNT on GO/Au and Au substrates, respectively. In both cases, the TIGERS signal is significantly stronger than TERS. Figure 3(c) shows the comparison of the Raman signals from different parts of the same CNT on GO/Au (CNT1-GO) and on Au (CNT1) substrates. The TIGERS signal of CNT1-GO is much stronger than TERS of CNT1. Similarly, Fig. 3(f) shows that the TIGERS signal of CNT1-GO is stronger than the TERS signal from a different CNT2. The results in Fig. 3 were obtained using the 638-nm excitation. On the other hand, weaker Raman signals and no significant difference between GO/Au and Au substrate was observed using 532-nm excitation. This could be explained by the better resonance matching of the GO band gap and laser energy for the 638-nm excitation, as discussed below.

B. TSD dependence of resonant (638 nm) and nonresonant (532 nm) excitation

Next, we investigated the TSD dependence of Raman signals of GO and CNT-GO systems under the resonant (638 nm) and nonresonant (532 nm) excitations to demonstrate the effect of the CT resonance in the CNT-GO system. We varied

the TSD from the classical (>10 nm) down to the quantum (<1 nm) regimes. We observed a transition from the classical to the quantum coupling, and more than four orders of magnitude signal enhancement with resonant excitation in the quantum regime.

Figure 4 shows the results of TSD measurements of GO and CNT3 on GO for 532 nm [Figs. 4(a)–4(d)] and 638 nm [Figs. 4(e)–4(h)] excitations. Figures 4(a)–4(d) show the expected TERS TSD dependence for 538-nm excitation, which is similar for both GO and CNT. Here, the TERS signal first increases with the decrease of TSD in the classical range of gap sizes (marked C). Then the TERS signal decreases for TSD in the quantum tunneling range (marked Q). This TERS quenching corresponds to the quantum limit of SERS due to tunneling [12,20]. The total gap size between the Au tip and Au substrate is ~ 2 nm and 4 nm for GO and CNT-GO junction, respectively. These results indicate the presence of quantum plasmonic effects in Au-GO-Au and Au-GO-CNT-Au systems at 532-nm excitation. Note that both the Raman signals of GO and CNT as well as the broad PL signal of Au decrease in the small gap range. However, a different situation is observed for 638-nm excitation.

In addition to tunneling, other effects may be present that modify the Raman signals, such as the reduction of the near field due to the electrical contact of CNT with the Au substrate, or when the RC time scale for the tip-sample junction becomes comparable to or shorter than an optical cycle. However, we believe that these effects play a minor role based on the specific tip-sample configuration of our setup, with the

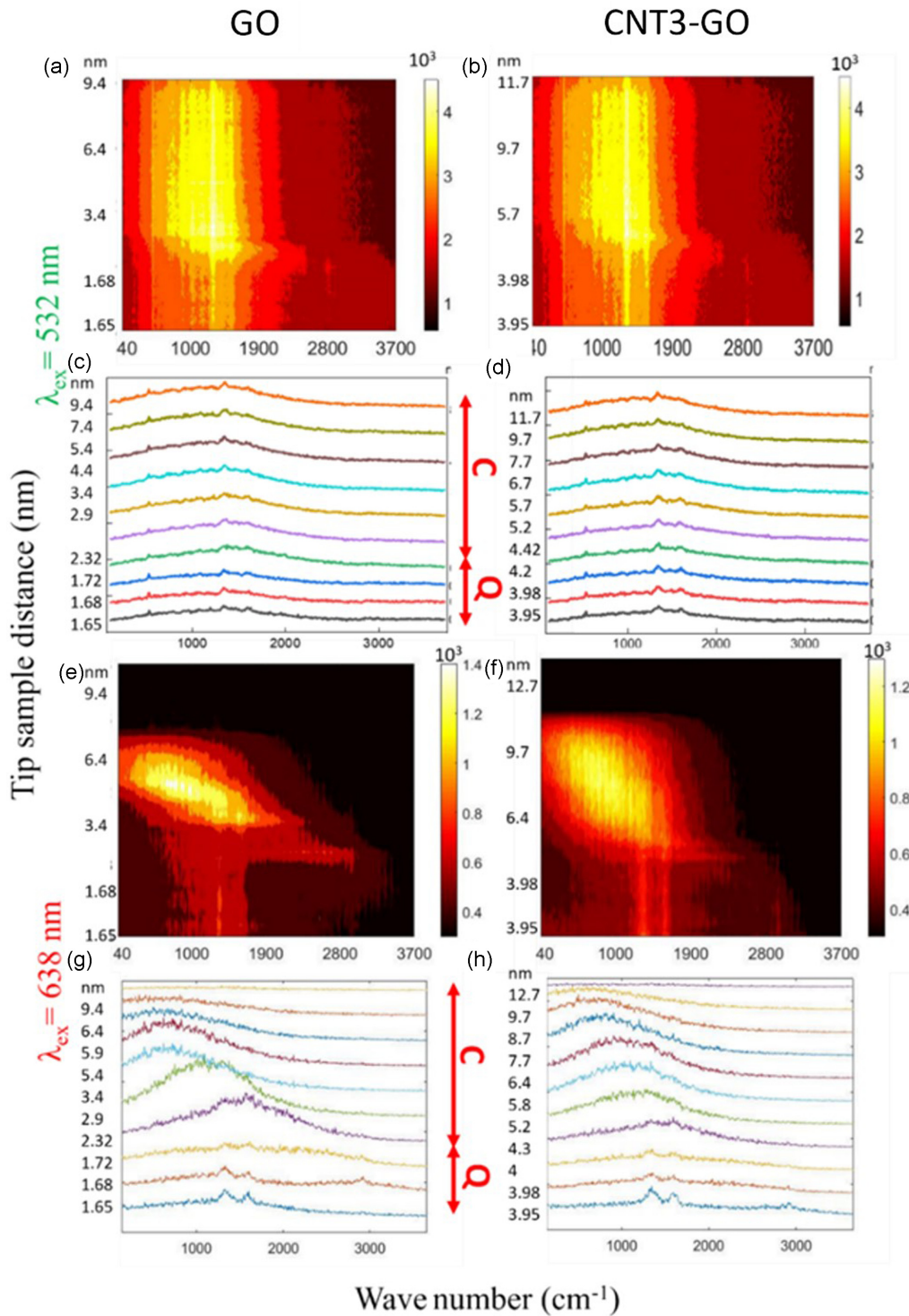


FIG. 4. TSD dependence of GO and CNT on GO for 532 nm (a)–(d) and 638 nm (e)–(h) excitations. The locations on GO and CNT correspond to the GO and CNT3-GO spots in Fig. 3(b), respectively. 2D contour maps (a),(b),(e),(f) and spectra (c),(d),(g),(h) reveal classical (C) and quantum (Q) regimes corresponding to large and small TSD, respectively.

small area of the tip-sample electrical contact compared to the tip size. The tip-sample configuration in our TERS setup is analogous to the SERS setup that was previously used to show the quantum tunneling limit [20].

Figures 4(e)–4(h) show that for 638-nm excitation there is a rise of the broad PL signal in the classical regime with decreasing TSD, which is steeper than for 532-nm excita-

tion. However, in contrast to the 532-nm excitation, there is no significant increase of the Raman signals until the vdW contact distance. After that there is a large increase of Raman signals with the decrease of TSD in the quantum regime, which is opposite the decrease observed due to tunneling for 532-nm excitation. The increase of the *G* band Raman signal from CNT is larger than from the GO in the quantum

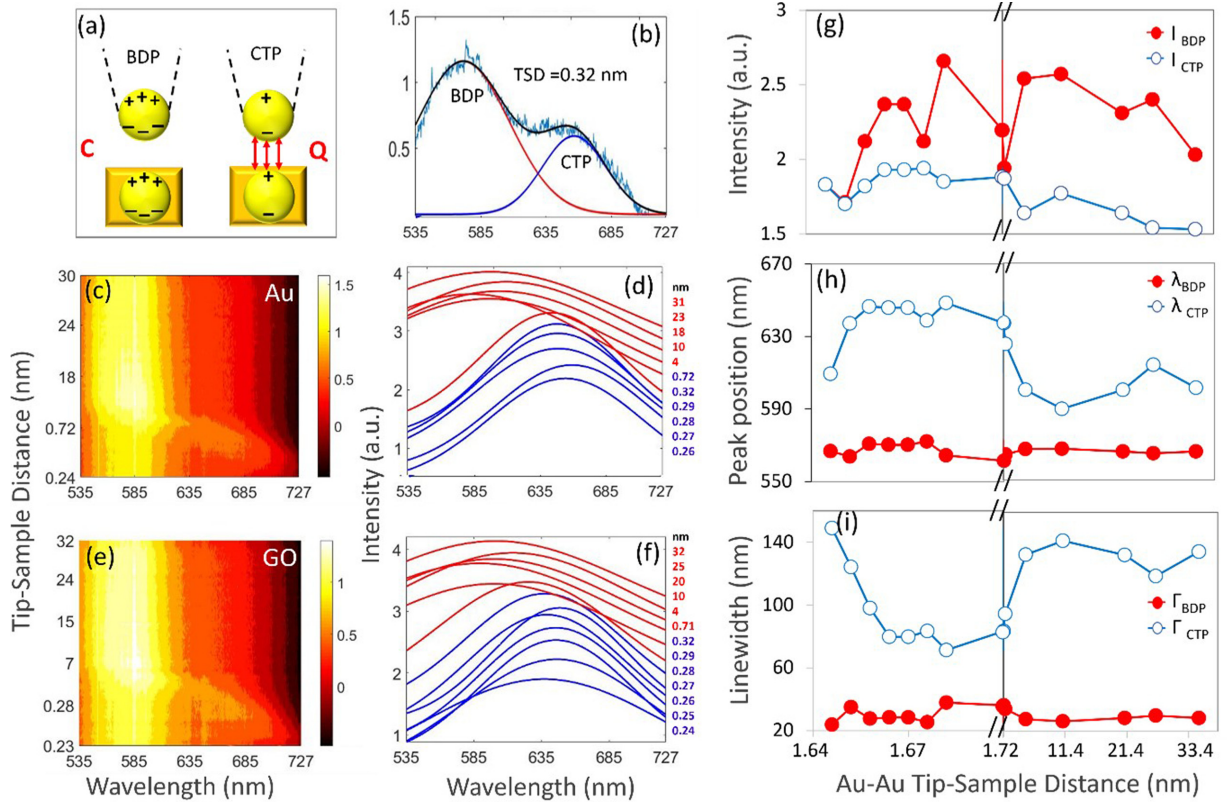


FIG. 5. TSD dependence for Au-Au and Au-GO-Au cavities using 532-nm excitation. (a) Schematic of two gap plasmon modes of the tip-substrate cavity (BDP and CTP). (b) PL spectrum at 0.32-nm TSD for the Au-GO-Au cavity with double Gaussian fitting of the two modes. Log intensity maps of TSD dependence of PL spectra of Au-Au (c) and Au-GO-Au (e) cavities. Fitted spectra for BDP mode in the classical (red lines) and CTP mode in the quantum (blue lines) regimes for the Au-Au (d) and Au-GO-Au (f) cavities. TSD dependence of the fitting parameters for the Au-GO-Au cavity: peak intensities (g), peak positions (h), and linewidths (i), respectively. TSD uncertainties before (0.16 nm) and after (10 pm) vdW contact.

regime as shown by the comparison of the maps in Figs. 4(e) and 4(f), respectively. Figure 4(f) shows two bright narrow lines emerging for smaller TSD after the decrease of the broad PL signal. A more detailed analysis of these signals is given in Supplemental Material Fig. S3 [52].

The broad PL signals for 638-nm excitation in Figs. 4(e) and 4(f) correspond to the TEPL of GO. We observed quenching of the GO PL in the tunneling range. This PL suppression in the quantum regime helps better resolve the Raman signals in the same spectral range.

C. Quantum plasmonic limit at 532-nm excitation

Next, we performed PL measurements with varying TSD at 532-nm excitation to demonstrate the traditional quantum plasmonic limit in the Au-Au cavity. We also performed PL measurements in the Au-GO-Au system and showed similar limiting behavior. These control experiments showed the evidence of the quantum plasmonic limit in TEPL of the cavity with the GO junction, which is overcome by the resonant 638-nm excitation.

Figure 5(a) shows the schematic of the bonding dipole plasmon (BDP) mode, formed by the image dipole coupling of the Au tip with the Au substrate in the classical regime. It also shows the charge transfer plasmon (CTP) mode that is generated by the tunneling in the quantum regime. The reduced number of charges at small gap size indicates the

reduced electric field. This corresponds to the quantum tunneling limit of the EM enhancement. Red arrows shown at the small gap indicate tunneling. Figure 5(b) shows the PL spectrum which consists of the two bands corresponding to these two modes.

Gaussian fitting was used to separate the TSD dependence of these modes for the Au-Au [Fig. 5(c)] and Au-GO-Au [Fig. 5(e)] systems. The fitted spectra are shown for the BDP band in the classical (red lines) and CTP band in the quantum (blue lines) regimes in Figs. 5(d) and 5(f) for the Au-Au and Au-GO-Au systems, respectively. The TSD dependence of the fitting parameters for the Au-GO-Au cavity including peak intensities (I_{BDP} , I_{CTP}), peak positions (λ_{BDP} , λ_{CTP}), and linewidths (Γ_{BDP} , Γ_{CTP}) are shown in Figs. 5(g)–5(i), respectively. The TSD dependence of the fitting parameters for the Au-Au cavity is shown in Supplemental Material Fig. S1.

The comparison of the TSD dependence for 532-nm excitation in Fig. 5 reveals that both Au-Au and Au-GO-Au cavities exhibit similar quantum plasmonic behavior. While quantum plasmonics in Au-Au systems was previously shown, we present a demonstration of quantum plasmonics with GO. Detailed analysis of the TSD dependence of the fitting parameters provides the supporting evidence. For example, Fig. 5(g) shows that the BDP mode intensity decreases with the decreasing gap size in the quantum regime of $d_{\text{gap}} < 1.72$ nm due to tunneling. The total gap includes the TSD of 0.32 nm

due to the vdW tip-sample contact and the 1.4 nm thickness of GO [see Fig. 2(e)].

The main quantum plasmonic signature is the blueshift of the CTP mode (blue line with empty circles) in Fig. 5(h) of more than 30 nm for TSD < 1.66 nm due to tunneling that is similar to quantum plasmonic resonances in Au-Au cavities [16,17]. The increased linewidth of this quantum plasmonic mode in Fig. 5(i) also supports the tunneling contribution.

D. Enhancement factors

Finally, we provide a detailed analysis of the enhancement factors for the PL and Raman signals in the classical and quantum regimes. We use the conventional definition of the classical enhancement factor (CEF) as [60]

$$\text{CEF} = \left(\frac{I_{\text{Tip In}}}{I_{\text{Tip Out}}} - 1 \right) \frac{S_{\text{FF}}}{S_{\text{NF}}}, \quad (1)$$

where $I_{\text{Tip In}}$ and $I_{\text{Tip Out}}$ are the signal intensities with the tip in contact and out of contact with the sample, respectively. S_{NF} and S_{FF} are the effective surface areas that generate the near-field (NF) and far-field (FF) signals, respectively.

In the classical regime, we obtain the far-field signal as $I_{\text{Tip Out}}$ and the mixture of near-field and far-field signals as $I_{\text{Tip In}}$. We assume that the near-field signal at TSD of vdW contact is generated by the hot spot at the tip apex with the radius of curvature of ~ 10 nm. On the other hand, the radius of the far-field excitation laser spot is ~ 500 nm. Assuming circular areas of πR^2 for both cases gives the value of $\frac{S_{\text{FF}}}{S_{\text{NF}}}$ of 2.5×10^3 [12]. The resulting CEF values of the PL and Raman signals for the 532- and 638-nm excitations are shown in Supplemental Material Figs. S3c, S3d and Figs. S3g, S3h, respectively.

In the quantum plasmonic regime, we consider the tunneling effect by using the near-field signal at the vdW contact TSD of 0.32 nm for I_{vdW} and the near-field signal at TSD < 0.32 nm as I_C , which approaches the conductive contact distance. The quantum EF (QEF) equation is

$$\text{QEF} = \left(\frac{I_C}{I_{\text{vdW}}} - 1 \right) \frac{S_{\text{vdW}}}{S_C}. \quad (2)$$

We assume that the signal enhancement at TSD < 0.32 nm originates from only a few atoms at the tip apex, in the limit from just one Au atom. Therefore, we use the radius of a Au atom of 0.179 nm to define the area S_C . For S_{vdW} we use the same area as above for the near field with the tip apex area of 10 nm. This gives the value of the $\frac{S_{\text{vdW}}}{S_C}$ factor of 1.2×10^4 . The resulting QEF values of the PL and Raman signals for the 532- and 638-nm excitations are shown in Supplemental Material Figs. S3a, S3b and Figs. S3e, S3f, respectively.

We used the Lennard-Jones model to perform the fitting of the tip-sample interaction as described above. We assumed the interaction of a single atom at the tip apex with the sample. If more atoms of the tip participate in the interaction, then it would lead to the overestimation of the QEF values. However, even if all the atoms of the 10-nm size tip area interact, that would reduce the QEF values by the $\frac{S_{\text{vdW}}}{S_C}$ factor, still giving ~ 2 – 3 times enhancement.

III. DISCUSSION

In this work, we present experimental demonstration of quantum plasmonics in the Au tip and Au substrate cavity with GO junction using TSD spatial and spectral shift dependence. This tunneling needs to be taken into consideration when performing TEPL or TERS imaging of GO, because it will set a fundamental limit on the signal enhancement that may be achieved by EM mechanism. Optimization of TSD needs to be performed to obtain the strongest signal.

Similarly, we obtained evidence for quantum plasmonics in the Au-GO-CNT-Au system. Figure 4(f) shows quenching of the GO PL due to the reduction of EM enhancement and increase of CNT Raman signal due to increased CM enhancement, supporting the TIGERS scheme in Fig. 1. Due to the GO substrate, there is an additional CNT Raman signal enhancement at short TSD. In the absence of the GO substrate the signal is lower as shown in the comparison of the signals in Figs. 2(c) (TERS) and 2(d) (TIGERS). The TIGERS signal shows more than four orders of magnitude enhancement at short TSD using the QEF analysis. Figure S3 shows the quenching of the PL signal at 532-nm excitation and the increase of the CNT Raman signals of the *G* and *D* bands in the quantum regime. There is a large increase of the *G*-band signal of TIGERS (solid line) compared to TERS (dashed line) in Fig. S3f. However, there is no significant difference between TIGERS and TERS for the *D* band, because GO makes a larger contribution to this band compared to CNT. The *G*-band intensity has a larger contribution of CNT and, therefore, shows a larger Raman signal enhancement at the decreasing TSD. We, therefore, demonstrate tunability of the CM mechanism by TSD, which is a different control parameter, that could be used for improving single-molecule imaging and biosensing.

In general, in the Au/Au experiments on the clean gold surfaces contacting at the 1–2 atom level it may be possible to short out the EM enhancement due to the classical electrical contact. This indeed happens when the contact area is large, as was shown, for example, for gradually merging plasmonic spheres, which showed a gradual transition from the classical to the quantum regime and further to the classical conducting regime [17,18]. We do not expect such a classical conductive contact based on a positive gap of more than 0.2 nm and only 1–2 atoms contact area.

In summary, we investigated the TSD dependence of the chemical mechanism of CNT on a hybrid GO/Au substrate in the quantum regime using a different tip-sample configuration (TIGERS). We showed that our system behaves predominantly based on EM at large TSD [Fig. 1(a)] and based on CM at small TSD [Fig. 1(b)]. The reason for that is that EM and CM have the opposite TSD dependence. The EM enhancement decreases with the decrease of TSD due to the tunneling, while the CM enhancement increases due to the larger wave-function overlap between GO and CNT, increasing the efficiency of charge transfer. Therefore, we used TSD as a control tool for separating the EM and CM effects. Our results may be generalized to other molecular systems beyond CNT that are in resonance with GO such as molecular dyes (methylene blue, cyanines) and biomolecular chromophores (heme, chlorophyll) in the visible spectral range. The

extension to biomolecules may be realized using hybrid substrates based on GO and aluminum substrate instead of gold in the near ultraviolet spectral range [61]. TIGERS signal

depends sensitively on the energetic alignment between the substrate (GO) and analyte (CNT). Therefore, the properties of the substrate should be tuned for a particular application.

- [1] *Surface-Enhanced Raman Scattering: Physics and Applications*, edited by K. Kneipp, M. Moskovits, and H. Kneipp (Springer-Verlag, Berlin, 2006).
- [2] E. Le Ru and P. Etchegoin, *Principles of Surface-Enhanced Raman Spectroscopy and Related Plasmonic Effects* (Elsevier, New York, 2008).
- [3] S. Schlücker, *Surface Enhanced Raman Spectroscopy: Analytical, Biophysical and Life Science Applications* (John Wiley & Sons, New York, 2011).
- [4] R. Zhang, Y. Zhang, Z. C. Dong, S. Jiang, C. Zhang, L. G. Chen, L. Zhang, Y. Liao, J. Aizpurua, Y. Luo *et al.*, Chemical mapping of a single molecule by plasmon-enhanced raman scattering, *Nature (London)* **498**, 82 (2013).
- [5] N. Tallarida, J. Lee, and V. A. Apkarian, Tip-Enhanced raman spectromicroscopy on the angstrom Scale: Bare and co-terminated ag tips, *ACS Nano* **11**, 11393 (2017).
- [6] J. Lee, K. T. Crampton, N. Tallarida, and V. A. Apkarian, Visualizing vibrational normal modes of a single molecule with atomically confined light, *Nature (London)* **568**, 78 (2019).
- [7] P. Alonso-González, P. Albella, M. Schnell, J. Chen, F. Huth, A. García-Etxarri, F. Casanova, F. Golmar, L. Arzubiaga, L. E. Hueso *et al.*, Resolving the electromagnetic mechanism of surface-enhanced light scattering at single hot spots, *Nat. Commun.* **3**, 684 (2012).
- [8] M. Moskovits, Surface-Enhanced spectroscopy, *Rev. Mod. Phys.* **57**, 783 (1985).
- [9] G. C. Schatz and R. P. Van Duyne, Image field theory of enhanced raman scattering by molecules adsorbed on metal Surfaces: Detailed comparison with experimental results, *Surf. Sci.* **101**, 425 (1980).
- [10] H. Xu, L. Xie, H. Zhang, and J. Zhang, Effect of graphene fermi level on the raman scattering intensity of molecules on graphene, *ACS Nano* **5**, 5338 (2011).
- [11] L. Jensen, C. M. Aikens, and G. C. Schatz, Electronic structure methods for studying surface-enhanced raman scattering, *Chem. Soc. Rev.* **37**, 1061 (2008).
- [12] Y. Zhang, D. V. Voronine, S. Qiu, A. M. Sinyukov, M. Hamilton, Z. Liege, A. V. Sokolov, Z. Zhang, and M. O. Scully, Improving resolution in quantum subnanometre-gap tip-enhanced raman nanoimaging, *Sci. Rep.* **6**, 25788 (2016).
- [13] K.-C. Lee, S.-J. Lin, C.-H. Lin, C.-S. Tsai, and Y.-J. Lu, Size effect of ag nanoparticles on surface plasmon resonance, *Surf. Coat. Technol.* **202**, 5339 (2008).
- [14] R. J. Green, J. Davies, M. C. Davies, C. J. Roberts, and S. J. B. Tendler, Surface plasmon resonance for real time in situ analysis of protein adsorption to polymer surfaces, *Biomaterials* **18**, 405 (1997).
- [15] W. Zhu, R. Esteban, A. G. Borisov, J. J. Baumberg, P. Nordlander, H. J. Lezec, J. Aizpurua, and K. B. Crozier, Quantum mechanical effects in plasmonic structures with subnanometre gaps, *Nat. Commun.* **7**, 1 (2016).
- [16] J. Zuloaga, E. Prodan, and P. Nordlander, Quantum description of the plasmon resonances of a nanoparticle dimer, *Nano Lett.* **9**, 887 (2009).
- [17] K. J. Savage, M. M. Hawkeye, R. Esteban, A. G. Borisov, J. Aizpurua, and J. J. Baumberg, Revealing the quantum regime in tunnelling plasmonics, *Nature (London)* **491**, 574 (2012).
- [18] J. A. Scholl, A. García-Etxarri, A. L. Koh, and J. A. Dionne, Observation of quantum tunneling between two plasmonic nanoparticles, *Nano Lett.* **13**, 564 (2013).
- [19] M. S. Tame, K. R. McEnery, Ş. Özdemir, J. Lee, S. A. Maier, and M. S. Kim, Quantum plasmonics, *Nat. Phys.* **9**, 329 (2013).
- [20] W. Zhu and K. B. Crozier, Quantum mechanical limit to plasmonic enhancement as observed by surface-enhanced raman scattering, *Nat. Commun.* **5**, 5228 (2014).
- [21] V. Kravtsov, S. Berweger, J. M. Atkin, and M. B. Raschke, Control of plasmon emission and dynamics at the transition from classical to quantum coupling, *Nano Lett.* **14**, 5270 (2014).
- [22] V. Kulkarni and A. Manjavacas, Quantum effects in charge transfer plasmons, *ACS Photonics* **2**, 987 (2015).
- [23] Z. He, Z. Han, J. Yuan, A. M. Sinyukov, H. Eleuch, C. Niu, Z. Zhang, J. Lou, J. Hu, D. V. Voronine *et al.*, Quantum plasmonic control of trions in a picocavity with monolayer WS₂, *Sci. Adv.* **5**, 10 (2019).
- [24] D. Xu, X. Xiong, L. Wu, X.-F. Ren, C. E. Png, G.-C. Guo, Q. Gong, and Y.-F. Xiao, Quantum Plasmonics: New opportunity in fundamental and applied photonics, *Adv. Opt. Photonics* **10**, 703 (2018).
- [25] C. Ciraci, R. T. Hill, J. J. Mock, Y. Urzhumov, A. I. Fernández-Domínguez, S. A. Maier, J. B. Pendry, A. Chilkoti, and D. R. Smith, Probing the ultimate limits of plasmonic enhancement, *Science* **337**, 1072 (2012).
- [26] L. Wu, H. Duan, P. Bai, M. Bosman, J. K. Yang, and E. Li, Fowler–Nordheim tunneling induced charge transfer plasmons between nearly touching nanoparticles, *ACS Nano* **7**, 707 (2013).
- [27] L. Wu, S. F. Tan, M. Bosman, J. K. Yang, C. A. Nijhuis, and P. Bai, Charge transfer plasmon resonances across silver–molecule–silver Junctions: Estimating the terahertz conductance of molecules at near-Infrared frequencies, *RSC Adv.* **6**, 70884 (2016).
- [28] S. F. Tan, L. Wu, J. K. Yang, P. Bai, M. Bosman, and C. A. Nijhuis, Quantum plasmon resonances controlled by molecular tunnel junctions, *Science* **343**, 1496 (2014).
- [29] S. Lerch and B. M. Reinhard, Quantum Plasmonics: Optical monitoring of dna-mediated charge transfer in plasmon rulers, *Adv. Mater.* **28**, 2030 (2016).
- [30] J. G. Simmons, Generalized formula for the electric tunnel effect between similar electrodes separated by a thin insulating film, *J. Appl. Phys.* **34**, 1793 (1963).
- [31] E. Burstein, Y. J. Chen, C. Y. Chen, S. Lundquist, and E. Tosatti, Giant” raman scattering by adsorbed molecules on metal surfaces, *Solid State Commun.* **29**, 567 (1979).
- [32] A. Otto, Surface enhanced raman scattering (SERS), what do we Know? *Appl. Surf. Sci.* **6**, 309 (1980).
- [33] J. R. Lombardi, R. L. Birke, T. Lu, and J. Xu, Charge-Transfer theory of surface enhanced raman Spectroscopy: Herzberg–teller contributions, *J. Chem. Phys.* **84**, 4174 (1986).

- [34] S. M. Morton, D. W. Silverstein, and L. Jensen, Theoretical studies of plasmonics using electronic structure methods, *Chem. Rev.* **111**, 3962 (2011).
- [35] I. Alessandri and J. R. Lombardi, Enhanced raman scattering with dielectrics, *Chem. Rev.* **116**, 14921 (2016).
- [36] X. X. Han, W. Ji, B. Zhao, and Y. Ozaki, Semiconductor-Enhanced raman Scattering: Active nanomaterials and applications, *Nanoscale* **9**, 4847 (2017).
- [37] J. D. Fowler, M. J. Allen, V. C. Tung, Y. Yang, R. B. Kaner, and B. H. Weiller, Practical chemical sensors from chemically derived graphene, *ACS Nano* **3**, 301 (2009).
- [38] J. T. Robinson, F. K. Perkins, E. S. Snow, Z. Wei, and P. E. Sheehan, Reduced graphene oxide molecular sensors, *Nano Lett.* **8**, 3137 (2008).
- [39] B. Meshginqalam, M. Ahmadi, R. Ismail, and A. Sabatyan, Graphene/Graphene oxide-based ultrasensitive surface plasmon resonance biosensor, *Plasmonics* **12**, 1991 (2017).
- [40] X. Ling, L. Xie, Y. Fang, H. Xu, H. Zhang, J. Kong, M. S. Dresselhaus, J. Zhang, and Z. Liu, Can graphene be used as a substrate for raman Enhancement? *Nano Lett.* **10**, 553 (2010).
- [41] A. Jabłońska, A. Jaworska, M. Kasztelan, S. Berbec, and B. Palys, Graphene and graphene oxide applications for SERS sensing and imaging, *Curr. Med. Chem.* **26**, 6878 (2019).
- [42] W. Su, N. Kumar, A. Krayev, and M. Chaigneau, In situ topographical chemical and electrical imaging of carboxyl graphene oxide at the nanoscale, *Nat. Commun.* **9**, 1 (2018).
- [43] D. Sun, M. Tang, L. Zhang, B. G. Falzon, D. B. Padmanaban, D. Mariotti, P. Maguire, H. Xu, M. Chen, and D. Sun, Microplasma assisted synthesis of gold nanoparticle/graphene oxide nanocomposites and their potential application in SERS sensing, *Nanotechnology* **30**, 455603 (2019).
- [44] L. Wang, Y. Zhang, Y. Yang, and J. Zhang, Strong dependence of surface enhanced raman scattering on structure of graphene oxide film, *Materials* **11**, 7 (2018).
- [45] Y. Song, K. Qu, C. Zhao, J. Ren, and X. Qu, Graphene Oxide: Intrinsic peroxidase catalytic activity and its application to glucose detection, *Adv. Mater.* **22**, 2206 (2010).
- [46] J. Zhang and X. S. Zhao, Conducting polymers directly coated on reduced graphene oxide sheets as high-performance supercapacitor electrodes, *J. Phys. Chem. C* **116**, 9 (2012).
- [47] D. Hernández-Sánchez, M. Scardamaglia, S. Saucedo-Anaya, C. Bittencourt, and M. Quintana, Exfoliation of graphite and graphite oxide in water by chlorin E6, *RSC Adv.* **6**, 66634 (2016).
- [48] G. Zhao, J. Li, X. Ren, C. Chen, and X. Wang, Few-Layered graphene oxide nanosheets as superior sorbents for heavy metal ion pollution management, *Environ. Sci. Technol.* **45**, 10454 (2011).
- [49] J. R. Lombardi and R. L. Birke, Theory of surface-enhanced raman scattering in semiconductors, *J. Phys. Chem. C* **118**, 11120 (2014).
- [50] D. V. Voronine, G. Lu, D. Zhu, and A. Krayev, Tip-Enhanced raman scattering of MoS₂, *IEEE J. Sel. Top. Quantum Electron.* **23**, 138 (2017).
- [51] S. Ambardar, R. Kamh, Z. Withers, P. Sahoo, and D. V. Voronine, Coupling nanobubbles in 2D lateral heterostructures, *Nanoscale* **14**, 8050 (2022).
- [52] See Supplemental Material at <http://link.aps.org/supplemental/10.1103/PhysRevB.106.035410> for supplemental figures.
- [53] C. Tang, Z. He, W. Chen, S. Jia, J. Lou, and D. V. Voronine, Quantum plasmonic hot-electron injection in lateral WSe₂/MoSe₂ heterostructures, *Phys. Rev. B* **98**, 041402(R) (2018).
- [54] D. R. Dreyer, S. Park, C. W. Bielawski, and R. S. Ruoff, The chemistry of graphene oxide, *Chem. Soc. Rev.* **39**, 228 (2010).
- [55] Y. Zhu, S. Murali, W. Cai, X. Li, J. W. Suk, J. R. Potts, and R. S. Ruoff, Graphene and graphene Oxide: Synthesis, Properties, and applications, *Adv. Mater.* **22**, 3906 (2010).
- [56] K. P. Loh, Q. Bao, G. Eda, and M. Chhowalla, Graphene oxide as a chemically tunable platform for optical applications, *Nat. Chem.* **2**, 1015 (2010).
- [57] G. Eda, C. Mattevi, H. Yamaguchi, H. Kim, and M. Chhowalla, Insulator to semimetal transition in graphene oxide, *J. Phys. Chem. C* **113**, 15768 (2009).
- [58] A. Bhattarai, A. Krayev, A. Temiryazev, D. Evplov, K. T. Crampton, W. P. Hess, and P. Z. El-Khoury, Tip-Enhanced raman scattering from nanopatterned graphene and graphene oxide, *Nano Lett.* **18**, 4029 (2018).
- [59] A. C. Ferrari, J. C. Meyer, V. Scardaci, C. Casiraghi, M. Lazzeri, F. Mauri, S. Piscanec, D. Jiang, K. S. Novoselov, S. Roth *et al.*, Raman Spectrum of Graphene and Graphene Layers, *Phys. Rev. Lett.* **97**, 187401 (2006).
- [60] B. Pettinger, P. Schambach, C. J. Villagómez, and N. Scott, Tip-Enhanced raman Spectroscopy: Near-fields acting on a few molecules, *Annu. Rev. Phys. Chem.* **63**, 379 (2012).
- [61] S. Ambardar, D. Nguyen, G. Binder, Z. W. Withers, and D. V. Voronine, Quantum leap from gold and silver to aluminum nanoplasmonics for enhanced biomedical applications, *Appl. Sci.* **10**, 4210 (2020).